






Vacuum breakdown in magnetic dipole wave by 10-PW class lasersE. S. Efimenko ¹, A. V. Bashinov ¹, A. A. Muraviev ¹, V. D. Volokitin,² I. B. Meyerov,²
G. Leuchs ^{1,3}, A. M. Sergeev,¹ and A. V. Kim ¹¹*Institute of Applied Physics, Russian Academy of Sciences, 603950 Nizhny Novgorod, Russia*²*Lobachevsky State University of Nizhni Novgorod, Department of Mathematical Software and Supercomputing Technologies, 603950 Nizhny Novgorod, Russia*³*Max Planck Institute for the Science of Light, 91058 Erlangen, Germany*

(Received 30 September 2021; accepted 13 June 2022; published 11 July 2022)

The vacuum breakdown by 10-PW-class lasers is studied in the optimal configuration of laser beams in the form of an m-dipole wave, which maximizes the magnetic field. Using 3D PIC simulations we calculated the threshold of vacuum breakdown, which is about 10 PW. We examined in detail the dynamics of particles and identified particle trajectories which contribute the most to vacuum breakdown in such highly inhomogeneous fields. We analyzed the dynamics of the electron-positron plasma distribution on the avalanche stage. It is shown that the forming plasma structures represent concentric toroidal layers and the interplay between particle ensembles from different spatial regions favors vacuum breakdown. Based on the angular distribution of charged particles and gamma photons a way to experimentally identify the process of vacuum breakdown is proposed.

DOI: [10.1103/PhysRevE.106.015201](https://doi.org/10.1103/PhysRevE.106.015201)**I. INTRODUCTION**

In the 1960s, in the early era of high-power lasers, optical breakdown in gases was a key issue of high-intensity laser-matter interaction, raising hopes to achieve extreme states of matter (see, e.g., Ref. [1] and references therein). Nowadays advances in the developing multipetawatt laser facilities [2] make it possible to put on the agenda the issue of vacuum breakdown, that is, the laboratory creation of dense electron-positron pair plasma, which until now could only be formed under extreme astrophysical conditions [3,4]. Undoubtedly, the solution of such a problem is a challenge to modern experimental technology, which can be solved in various forms of experimental implementation and, in particular, different configurations of optical fields, in which various dynamic modes of interaction and, accordingly, states of matter can be created.

By analogy with optical breakdown there are two main mechanisms of plasma production. In the case of optical breakdown these mechanisms are field ionization of atoms or molecules and avalanche ionization by electron impact. In the case of vacuum breakdown the two mechanisms are direct tunneling ionization of vacuum by laser fields and quantum electrodynamic (QED) cascade. Direct tunneling ionization requires the values of fields commensurate with the Schwinger field [5], corresponding to an intensity of 4×10^{29} W/cm². Recently, it was claimed that this threshold can be decreased down to an intensity of about 10^{27} W/cm² [6–8], which is still unattainable for the currently foreseeable laser powers. The mechanism of quantum electrodynamic (QED) cascade [9] assumes that an electron accelerated in a laser field emits a gamma photon, which, in turn, decays in a strong laser field into a pair of an electron and a positron.

Under certain conditions this process can be repeated and therefore it can result in the avalanche mode of vacuum ionization [10–12]. Ultimately, a dense pair plasma can be created, in which plasma structures and their properties substantially depend on the configuration of the electric and magnetic fields [7,13–24].

The main research done so far was devoted to laser field configurations that maximize the electric field. An ultimate example of such a configuration is the limiting case of a multi-beam setup in the form of a converging e-dipole wave [25,26], where the focal volume is minimal and the electric field is highest. Such a configuration is favorable for minimizing the vacuum breakdown threshold power for self-sustained QED cascade development, and the threshold power lies below 10 PW [27], which makes it very promising for upcoming experimental facilities. However, it should also be kept in mind that not only the breakdown threshold, but also the properties of the created plasma states substantially depend on the laser field configuration. For example, the mentioned multibeam laser configuration corresponding to a converging e-dipole wave makes it possible to create extreme current structures elongated along the virtual dipole orientation. This may result in unbounded electron-positron plasma contraction in the form of current sheet formation [28] or pinching [29], opening the door to creating quantum pair plasma and approaching the Schwinger field.

In this paper we consider the converging m-dipole wave that maximizes the magnetic field in the focus. In particular, we unveil the physics of the vacuum breakdown effect in ultra-high-power laser fields of such structure. We show that the plasma structures forming as a result of a QED cascade represent concentric toroidal layers around the central magnetic axis, which significantly contrasts with the plasma column

formed in the case of an e-dipole wave. Based on individual dynamics of particles studied in detail in Ref. [30] we show that although an electron or a positron can gain less energy in the m-dipole wave than in the e-dipole wave of the same power, the stronger magnetic field of the m-dipole wave can intensify gamma radiation. As a result, although the m-dipole wave is not as optimal for QED cascade development as the e-dipole wave, the threshold power of the vacuum breakdown and the avalanche growth rate in these types of waves are close. An important feature of such a configuration is that charged particle motion can be expected to produce current-plasma structures leading to extreme states similar to a θ pinch by analogy with a z pinch in the case of an e-dipole wave. This fact can significantly increase the interest in laser fields producing such magnetic structures from the point of view of laboratory modeling of astrophysical phenomena, which are usually associated with astrophysical objects with super-strong magnetic fields, such as neutron stars and magnetars [31–33].

This paper is organized as follows. In Sec. II we define the problem and briefly describe the distributions of the electric and magnetic fields of a standing m-dipole wave, which is important for understanding of the individual dynamics of particles. In Sec. III we discuss in detail individual trajectories of charged particles and gamma photons characteristic for vacuum breakdown in a given field of a standing m-dipole wave. In Sec. IV we consider the space-time structure of the vacuum breakdown. In particular, we define the inner region and the outer region and discuss the influence of these regions on QED cascade development. In Sec. V we describe angular and energy properties of particles. The vacuum breakdown threshold is estimated numerically and analytically in Sec. VI. In Sec. VII the possibilities of the experimental observation of vacuum breakdown are discussed. Finally, in Sec. VIII the conclusions are summarized.

II. PROBLEM STATEMENT

A. General view

The vacuum breakdown threshold is a laser wave power at which particle generation due to QED cascade development and particle escape from the interaction region completely compensate each other, so that the overall particle production rate is zero. Above this threshold the number of particles in the interaction region grows exponentially, paving the way for creation of dense pair plasma. From the experimental point of view the threshold power value is one of the key characteristics of the proposed laser field structure, because it defines the minimal power required to induce the process of vacuum breakdown.

Even future experimental facilities impose a severe restriction on the maximum attainable power delivered in one or several ultra-intense laser beams, so it is extremely important to determine the structure of laser fields minimizing this threshold. The threshold can be reduced down to around 6 PW with help of 16 laser beams with a specific elliptic polarization [34]. In the more practical case of linear polarization, 12 laser beams mimicking a converging dipole wave can trigger vacuum breakdown at powers starting from approximately 10 PW

[27,28]. For an ideal e-dipole wave [25] the threshold amounts to 7 PW [27,28]. In this paper we show that although the breakdown threshold in the m-dipole wave is higher than in the e-dipole wave, it is still close to 10 PW, which makes this field structure worth considering at future experimental facilities. Another stimulus comes from the fact that the generated plasma structures can be qualitatively different as compared to the case of the e-dipole wave, so different regimes of interaction can be reached, thus enriching experimental means of exploring vacuum breakdown.

In order to determine the breakdown threshold we need to calculate the net production rate of electrons and positrons, which is the difference of the pair generation rate and the particle escape rate in highly inhomogeneous fields, as a function of the laser power. In optical breakdown an averaged description of particle motion can be used and particle escape is usually diffusive. In relativistically strong fields particle escape has to be calculated by direct simulation due to the complexity of the trajectories, which is especially important in strongly inhomogeneous fields. In this work the particle escape rate is determined by means of numerical simulations accounting for emission of gamma quanta, the decay of which in the regions of strong fields results in the production of electron-positron pairs. In contrast to the recent work [30], which considered a general analysis of particle dynamics, here we concentrate on laser powers near the breakdown threshold and present a more detailed picture of the particle trajectories that determine the breakdown threshold, as well as the structure of the distributions of the produced particles and their energy characteristics.

B. Field structure of the m-dipole wave

The exact analytical expressions for the standing fields of the m-dipole wave are given in Refs. [25,30]. The magnetic field has a poloidal structure, and the electric field is toroidal, both fields are axially symmetric. In Fig. 1(a) we present three-dimensional electric (red) and magnetic (blue) field distributions. In the coordinate system we have chosen the magnetic field has radial and axial components while the electric field only has an azimuthal component. In the focal region the magnetic field is directed predominantly along the z axis. The maximal amplitude of the magnetic field is achieved at the point $\rho = 0, z = 0$, which we will further refer to as the central point or the center of the wave, and is equal to

$$a_B = A_0 = 2F_0\sqrt{P}/3 \approx 780\sqrt{P}. \quad (1)$$

Here A_0 is the maximum amplitude of the magnetic field, which can be referred to as the amplitude of an m-dipole wave, $F_0 = \frac{2e}{mc^2} \sqrt{\frac{3}{c}} 10^{22} \text{ erg s}^{-1}$ and P is the total wave power normalized to 1 PW. The maximal amplitude of electric field a_E is achieved at the central plane, which is perpendicular to the z axis and contains the central point, at the points with distance from central point $\rho = 0.33\lambda$. This amplitude is equal to

$$a_E \approx 0.65A_0 \approx 510\sqrt{P}. \quad (2)$$

The z axis corresponds to the first node of the electric field. The second node resembles a spherical surface with radius

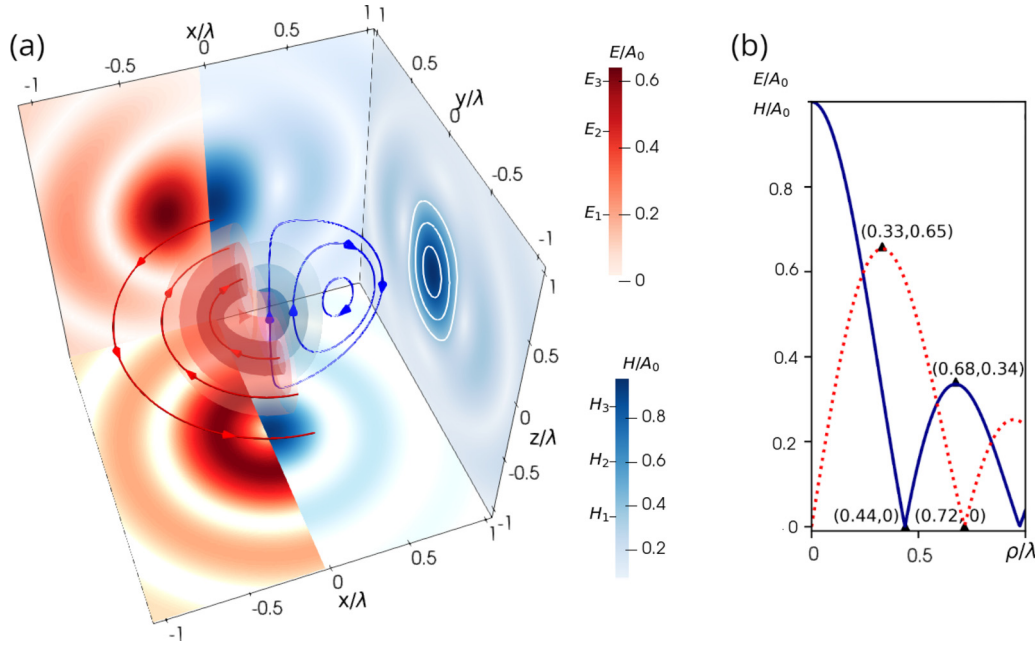


FIG. 1. (a) Spatial distribution of electric (left part of the cube, red) and magnetic (right part of the cube, blue) fields of the standing m-dipole wave. Volume contour surfaces depict the absolute values of fields, corresponding levels (E_1, E_2, E_3 and H_1, H_2, H_3) are shown in color bars. Concentric white contour levels at right cube face correspond to the same amplitude levels (H_1, H_2, H_3). Lines with arrows represent electric (red) and magnetic (blue) field lines in planes $z = 0$ and $y = 0$, respectively. Surfaces at cube faces represent corresponding field distribution in central sections $x = 0$, $y = 0$, $z = 0$, respectively. (b) Electric (dashed line) and magnetic (solid line) fields as function of ρ in the plane $z = 0$.

$r \approx 0.72\lambda$. The second antinode of the magnetic field with the amplitude $0.34a_B$ is at $\rho = 0.68\lambda$, as shown in Fig. 1(b).

C. Numerical setup

Avalanche-like production of electron-positron pairs is a compound process depending on the space-time structure of fields, particle and photon distributions, and their spectra. Therefore, the most rigorous method for analysis of this process is numerical simulations. For simulations we use the 3D QED-PIC code PICADOR [35] which has an Adaptive Event Generator [36] for modeling of photon emission and photon decay into electron-positron pairs in frame of the quasiclassical approach [37].

In series of simulations we consider the evolution of the electron-positron ensemble. Initially seed electrons and positrons are at rest and distributed uniformly within a sphere located in the focus of a continuous m-dipole wave. The radius of the sphere is equal to laser wavelength λ . The center of the sphere coincides with the central point. Fields of the m-dipole wave are set analytically [25,30] in order to omit the back reaction of generated electron-positron plasma. The initial number of macroparticles of each type (electron, positron) is 4×10^6 . Particle motion and QED-cascade development are simulated for a time interval of $20T$, where T is the laser wave period. The simulation box is $3\lambda \times 3\lambda \times 3\lambda$ along x , y , and z axes with cell number $192 \times 192 \times 192$. The time step is $T/300$ and can be automatically subdivided by the Adaptive Event Generator.

In order to determine the role of QED cascade we perform simulations with and without QED cascade taken into

account. In the latter case particles may emit photons and experience recoil, but photons are prohibited from decaying into electron-positron pairs.

III. KEY PARTICLE TRAJECTORIES FOR VACUUM BREAKDOWN

Vacuum breakdown is a process of avalanche-like production of electron-positron pairs in laser fields. For an avalanche to develop, the generation rate of new particles via QED cascades must be higher than the rate of particle escape from the high-field region [9]. In contrast to conventional gas or matter optical breakdown where the ionization rate can be expressed as a function of the local value of the electric field, in the case of vacuum breakdown particle motion plays a definitive role due to QED cascade development. Thus we start our consideration with a systematic study of those types of trajectories in the field of a magnetic dipole wave, which contribute the most to QED cascade development. To be more specific, in this section we consider different types of positron motion in a given field of an m-dipole wave. Taking into account that the positron is the antiparticle of the electron all conclusions made can be generalized to electron motion: the only difference is the opposite direction of azimuthal motion excited by the electric field.

According to the results obtained in our recent work [30], abundant pair production on the femtosecond time scale in fields of the m-dipole wave demands powers greater than 3 PW. Within the power range $1 \text{ PW} < P < 25 \text{ PW}$ where the threshold power value is expected the main regimes of motion are *ponderomotive trapping*, *radial anomalous radia-*

tive trapping (ART), and *normal radiative trapping* (NRT). In the regime of *ponderomotive trapping* particles oscillate around the z axis (the first node of the electric field) and drift along it outwards from the focus. In this regime particle energy is relatively low. In the *radial ART* regime particles are attracted from the first electric field node to the first electric field antinode in the radial direction due to radiation losses and drift along the z axis. In this region particles can gain the maximal energy and emit most energetic photons. After reaching the antinode region particles eventually leave it due to the influence of the centrifugal force and drift along the z axis. Particles released from *radial ART* can escape the focal region or be trapped due to radiation losses in the second electric field node. In this region particles move in the NRT regime, gyrating in a strong magnetic field and drifting towards the z axis along the spherical surface which corresponds to the second node. In this regime particle energies are much lower than energies in the ART regime and photons can be emitted in different directions including directions towards the center.

In order to reveal key regimes of motion during the avalanche-like pair production we analyze trajectories of particles generated as a result of the vacuum breakdown (see Fig. 2) in frame of the numerical setup described above. We choose the power of 20 PW at which breakdown is unambiguously triggered. The analysis has revealed that trajectories corresponding to *ponderomotive trapping* are not present during QED cascade development. The reason is that with increasing power the basin of *ponderomotive trapping* decreases in favor of *radial ART* [30]. Photons must decay very close to the z axis in order for generated particles to become ponderomotively trapped. Such photons must be emitted almost exactly towards the center and must not decay on the way. These facts significantly decrease the probability of appearance of new particles in the regime of ponderomotive trapping.

Simulations show that *radial ART* and NRT are the basic regimes of motion for the QED cascade. Most particles generated within the region of the electric field antinode either become trapped in the *radial ART* regime [trajectories 1, 2, 4, and 6 in Figs. 2(a) and 2(b)] or quickly (within approximately $0.5T$) escape the region at large angles to the z axis [trajectories 3 and 5 in Figs. 2(a) and 2(b)] due to the centrifugal force. In the antinode region one might distinguish two alternating stages of motion. At the first stage, when the electric field exceeds the magnetic field, the curvature of the particle trajectory is relatively small, so a particle is accelerated with negligible radiation losses and can gain energy up to $\gamma \sim a_E$. At the second stage, when the magnetic field becomes dominant, the curvature of the particle trajectory is significantly increased which can cause strong radiation losses. If a particle loses a large enough part of its energy due to photon emission, then the Larmor radius is significantly reduced and the particle can stay in the region for another half of the wave period drawing nearer the electric field antinode. Near the antinode particles are pushed away from the antinode region by the centrifugal force without losing a significant part of their energy. Thus, for a given particle escape time is approximately a whole number of wave half-periods. The closer a particle is to the z axis, the longer it takes for it to leave this region. For example, in Figs. 2(a) and 2(b) it is shown that trajectories

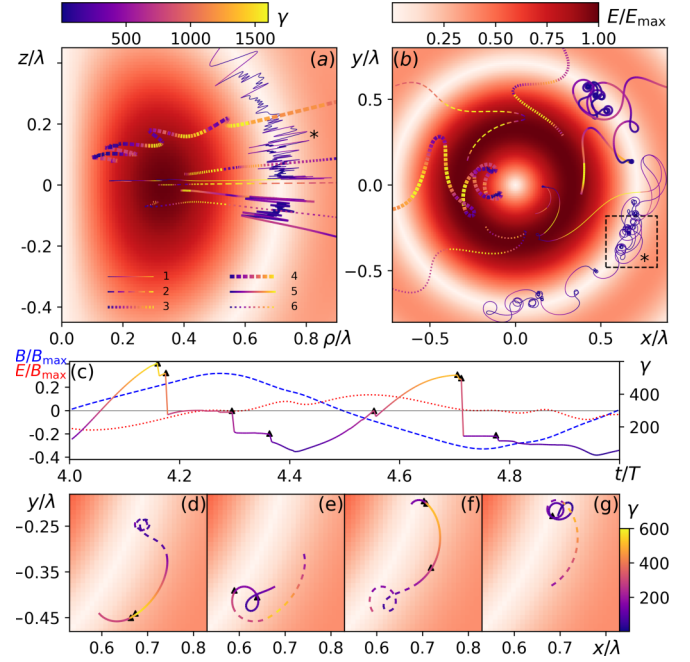


FIG. 2. Positron motion in fields of m-dipole wave. Different types of trajectories in coordinate space: (a) $z\rho$ space and (b) xy space. The color along trajectory demonstrates the particle's Lorentz factor. Distribution of normalized electric field amplitude is in shades of red as function of (a) z and ρ and (b) and (d)–(g) x and y in the plane $z = 0$. A more detailed view of positron motion close to the electric field node for a trajectory marked by asterisk in (a) and (b) is shown in (c)–(g). In panel (c) the solid multicolor line, dashed blue line and dotted red line indicate time evolution of the positron Lorentz factor, the z component of the magnetic field and the azimuthal electric field along trajectory, respectively. The solid line in each panel (d)–(g) corresponds to the positron trajectory during the quarter period in the upper panel (c). The dashed line shows part of the trajectory during previous quarter period. Triangle marks in (c) and corresponding marks in (d)–(g) indicate moments of emission of highly energetic photons. Region considered in (d)–(g) is highlighted by rectangle with dashed edge in (b).

1, 2, 4, and 6 of particles which took from $1T$ to $2.5T$ to escape the antinode region: each loop or U-turn corresponds to approximately $0.5T$.

When a particle leaves the antinode region, it enters the region where the magnetic field dominates. If a particle retains its energy $\gamma \sim a_E$, then it passes through this region because the maximum magnetic field there is $0.34a_B$ and the corresponding Larmor radius $a_E/(0.34a_Bk) \approx 0.3\lambda$ is sufficiently large. Such particles escape the focal region mainly at large angles to the z axis. In order to be trapped a particle must have a much smaller Larmor radius, which can result from energy reduction due to emission of one or several photons with a substantial part of the particle's energy. This trapping is the so called *normal radiative trapping* (NRT) [26]. From Figs. 2(a) and 2(b) it is clear that the energy of trapped particles (trajectories 1 and 5) is reduced much more significantly than that of transient ones (trajectories 2–4 and 6) at the second electric field node.

When trapped in the vicinity of the second electric field node [trajectories 1 and 5 in Figs. 2(a) and 2(b)], a particle shows random walking in the azimuthal direction and slow drifting along the sphere of the second electric field node towards the z axis. A particle may escape the trapped state if it gains a large enough energy and does not radiate gained energy. If the distance from a particle to the $z = 0$ plane is large enough ($z > 0.4\lambda$), then the escaped particle propagates at a small angle to the z axis, because farther from this plane the radial component of the magnetic field becomes comparable with the axial component and excites a large axial momentum. On average particles need approximately $4T$ to escape the trapped state.

In order to demonstrate photon emission by trapped particles and their impact on the QED cascade in the antinode region, we present typical particle motion in the NRT regime during a wave period [see Figs. 2(c)–2(g)]. The considered motion corresponds to the trajectory marked by an asterisk in Figs. 2(a) and 2(b).

During approximately the first quarter of the wave period the trapped particle is accelerated by the electric field in the vicinity of the electric field node [see Figs. 2(c) and 2(d)]. At the same time the growing magnetic field deflects the particle to the region with a stronger electric field, increasing the curvature of the trajectory and enhancing the emission of photons. Photon emission instances for this particular trajectory are marked by triangles in Figs. 2(c)–2(g). Deflection by magnetic field can occur in both directions: to the first or to the second electric field antinode. For the considered particle this results in clockwise motion in Fig. 2(d). The particle makes approximately a half-turn with the maximal distance from the node of about $\Delta\rho = cT/4\pi \approx 0.1\lambda$. At such distance the electric field amplitude is approximately $0.4a_E$, and thus a particle can gain a Lorentz factor up to $0.4a_E$. These estimates of maximal energy and particle shifts from the node are consistent with Figs. 2(a) and 2(c).

During the second quarter period [see Figs. 2(c) and 2(e)] the magnetic field reaches its maximum. Due to several photon emissions a particle loses a major part of its energy and rotates with a small Larmor radius, i.e., remains in the trapped state.

In the next half-period [see Figs. 2(c), 2(f), and 2(g)] the z component of the magnetic field changes its sign. As a result the particle's clockwise motion changes to counterclockwise motion. In other respects the particle's motion is similar to the first half-period. The particle is deflected to the region where the electric field is stronger, so it can regain energy up to $0.4a_E$ [see Figs. 2(c) and 2(f)]. The increased magnetic field stimulates photon emission so the particle rotates, emits a number of photons and its energy and Larmor radius are reduced; see Figs. 2(c) and 2(g). Thus each half a period the particle makes a step in the azimuthal direction. This step occurs in a random direction depending on the number of rotations at the second quarter-period. Changes of drift directions can be seen in Fig. 2(b) for the trajectory marked with an asterisk.

Also Figs. 2(d)–2(g) shows that, while trapped, a particle can emit photons in different directions, including the direction towards the center, and the energy of these photons can be comparable with the energy of parent particles [see Figs. 2(a) and 2(f)]. These gamma photons originated

in the vicinity of the second electric field node and emitted towards the center are of great importance because, while decaying in the antinode region, they can produce secondary particles that exhibit the regimes of motion described above.

Thus, ultimately, all trajectories escape the focus, but particles can be trapped for some period of time, facilitating the process of creation of new particles and decreasing the escape rate. The *radial* ART regime is very favorable for vacuum breakdown, because particles oscillate in the strong electric field region for several halves of the wave period and emit high-energy photons. At the same time there can be interplay between ART and NRT, which leads to a reduction of threshold power of the breakdown. Particles escaping from the strong electric field region can be trapped in the NRT regime. In turn, photons emitted in the NRT regime can propagate to the center and produce a pair which can get trapped in the ART regime. Also photons emitted in the ART regime can decay in the vicinity of the second electric field node (the basin of the NRT). As a result, vacuum breakdown can be nonlocal: photons generated in one region can propagate and decay in another region. The second node and the first antinode of the electric field have been identified as key regions for this interplay.

IV. THE SPACE-TIME STRUCTURE OF VACUUM BREAKDOWN

When vacuum breakdown occurs, the particle distribution in space and time is determined not only by particle motion but also by production of new particles. The latter factor may lead to a qualitative change of the particle distribution and, consequently, the dynamics of vacuum breakdown. To distinguish more clearly the impact of pair production from the impact of particle motion we compare particle and photon distributions with and without QED cascade taken into account at the wave power of 20 PW; see Fig. 3.

First, we consider plasma structures that are formed during QED cascade development. We show the distributions at the moments of time when particles are farthest from the center [see Fig. 3(a)] and closest to it [see Fig. 3(e)]. The particle structure consists of several concentric oscillating toroidal layers with the size along the z axis much less than the laser wavelength. Their location corresponds to the antinode and node regions, the role of which was discussed above. The space-time particle distribution highlights these regions more clearly. We will refer to these regions as the inner region (antinode) and the outer region (node). These regions are shown by rectangles with dashed edges in Figs. 3(a), 3(b), 3(e), and 3(f). We choose the cylindrical surface $\rho = 0.6\lambda$ as the boundary between the inner region and the outer region. For the inner layer this boundary corresponds to the most distant from the center position of the pair distribution maximum [see Fig. 3(a)]. For the outer layer the characteristic shift of trapped particles from the second electric field node $\rho = 0.72\lambda$ is approximately $\Delta\rho = 0.1\lambda$, as was obtained above (trajectories 1 and 5 in Fig. 2).

Within the inner region there are two toroidal layers with a boundary between them near the magnetic field node $\rho = 0.44\lambda$. The reasoning for this is that new particles accelerated

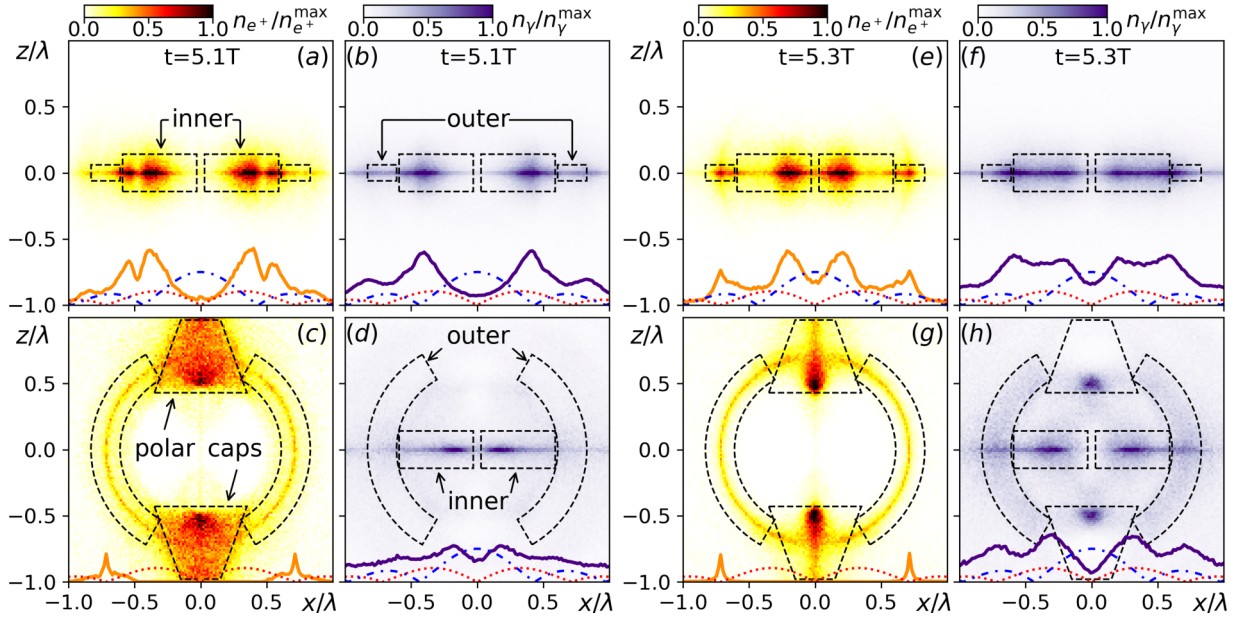


FIG. 3. Interaction of a standing m-dipole wave with seed particles at the wave power of $P = 20$ PW. Positron (a, c, e, g) and photon (b, d, f, h) density distributions normalized to their maxima at different moments of time with (a, b, e, f) and without (c, d, g, h) QED cascade taken into account. The dotted red and dash-dotted blue curves correspond to the distribution of electric and magnetic fields along the x axis, which contains the origin of coordinates. Solid orange and purple curves show photon and positron distributions along the same axis, respectively. Figures with dashed edges highlight different regions of particle and photon distributions.

by the electric field are deflected in opposite radial directions by the magnetic field at different sides of its node. The first layer consists of the particles which move in the ART regime or are going to escape the inner region, since particles near the electric field antinode $\rho = 0.33\lambda$ can be pushed out by the centrifugal force. For this reason the second layer corresponds to escaping particles.

In the outer region particles oscillate close to the first electric field node at $\rho = 0.72\lambda$. The simulations show that the greater the wave power, the more distinct the inner layers are as compared to the outer layer. Besides particles oscillating in the inner region and the outer region there are also escaping particles outside the outer region. The photon distribution also consists of several concentric toroidal layers [see Figs. 3(b) and 3(f)] and in a similar manner this distribution oscillates along the radius.

Note that spatial distributions of escaping particles and photons are modulated at the double wave frequency because, as shown in the previous section, the escape time for a given particle is close to a multiple of half of the wave period and radiation losses are intensified each half of wave period.

In the case without QED cascade after approximately $5T$ after the start of particle motion there is only the outer layer and there are no inner layers. By this time particles are released from the ART regime in the inner region and either escape the focal region or become trapped in the outer region. Particles trapped in the outer region oscillate in the vicinity of the second electric field node and drift towards the z axis, thus the particle distribution represents a spherical layer [see Figs. 3(c) and 3(g)] with polar caps at the intersection with the z axis. At the polar caps, where both electric and magnetic fields are weak, particles form bunches, which periodically contract and expand, and are gradually expelled in a cone

around the z axis with an opening angle around 40 degrees. Though the particle distributions are different, photon distributions are quite similar in the cases with [see Fig. 3(b) and 3(f)] and without [see Figs. 3(d) and 3(h)] QED cascades especially in the vicinity of the plane $z = 0$: In both cases inner and outer layers are present. Even without QED cascade there are photons propagating to the center of the m-dipole wave from the second electric field node. Like in the case with QED cascade, the photon distribution has a small width along the z axis in the inner region. Such photons can decay near the center producing new pairs, and the correlation of spatial distributions of particles and photons in Figs. 3(e) and 3(h) confirms this.

Thus, the comparison of distributions in Fig. 3 gives clear evidence of how the QED cascade qualitatively changes distributions of electrons and positrons. First, it is shown that the inner layers are a consequence of cascade development. Second, cascade growth is faster near the plane $z = 0$ due to a slower drift of particles along the z axis and a higher probability of photon decay. As a result, the particle distribution is more compact along the z axis in the case when the QED cascade is taken into account. Even at the second electric field node we can observe only a small spherical sector [see Fig. 3(e)], not a large part of a sphere like in Figs. 3(c) and 3(g). Third, the complex interplay between the antinode and node regions is confirmed.

V. ENERGY AND ANGULAR SPECTRA OF PARTICLES AND PHOTONS

In previous sections we analyzed particle trajectories and dynamics of pair distributions in space and time during the development of QED cascades in fields of a standing m-

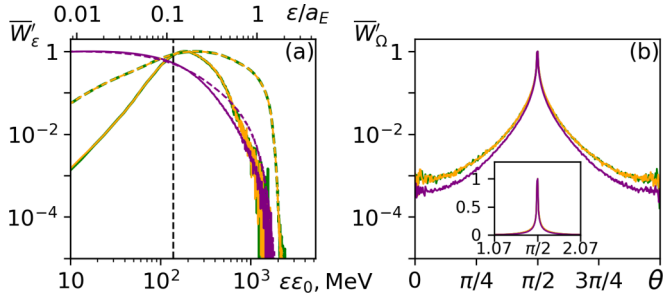


FIG. 4. (a) Energy and (b) angular averaged spectra of electrons (green line), positrons (orange line), and photons (purple line) in the field of the m-dipole wave with power 20 PW. Solid lines correspond to spectra of particles crossing the observation sphere with radius $r = 1.5\lambda$ averaged over the wave period. Dashed lines show averaged energy spectra in the whole simulation box. The inset in panel (b) demonstrates angular distributions of particles and photons on a linear scale. Lines corresponding to photons and particles in the inset overlap. Bottom and top axes in panel (a) show dimensional and dimensionless energy ranges, respectively, $a_E \approx 2280$. Vertical dashed line in panel (a) denotes the maximum of the averaged energy distribution obtained in the case without QED cascade taken into account.

dipole wave. Based on this we consider angular and energy distributions of charged particles and photons. In order to reveal the influence of QED cascade on such characteristics we analyze spectra of charged particles and photons in the whole simulation box and spectra of particles and photons crossing the observation sphere with a radius of 1.5λ . At such distances from the center photon decay, as well as emission of high-energy photons, are noticeably suppressed.

In order to obtain energy and angular distributions we apply the same procedure as used in Ref. [30]. Let $I'_\Omega \equiv \frac{dI}{d\Omega}$ denote the fraction of energy dI of particles or photons in the simulation box (or passing through the observation sphere) with momentum directed into an element of solid angle $d\Omega$ in the momentum space. Note that the angular distribution in momentum space measured in the micron-sized region is relevant to the angular distribution in coordinate space at a large distance, where the experimental detectors are usually placed. The normalizing factor is equal to $I_{\Omega,n} = \int I'_\Omega d\Omega$. The normalized energy of particles or photons per solid angle over time period $l\Delta t$ is $W'_\Omega = \sum_{j=0}^l I'_\Omega(t_0 + j\Delta t) / I_{\Omega,n}(t_0 + j\Delta t)$, where l is the integral number. Finally, averaged angular distributions of particles or photons are $\bar{W}'_\Omega = W'_\Omega / W'_{\Omega,\max}$. In simulations $t_0 = 18T$, $\Delta t = T/24$ and $l = 48$. The distribution of \bar{W}'_Ω is uniform along the azimuthal angle owing to the symmetry of the field structure, thus we analyze it with respect to the polar angle θ measured from the positive direction of the z axis. By analogy with \bar{W}'_Ω the averaged relative energy distribution \bar{W}'_ε can be introduced by replacing Ω with the particle (photon) dimensionless energy ε , which is the electron energy normalized to the rest electron energy ε_0 .

Retrieved energy and angular distributions are shown in Fig. 4. Note that electron (green curve) and positron (orange curve) distributions overlap in Fig. 4. The averaged energy distribution of particles passing through the observation sphere (mainly escaping particles) differs from the energy

distribution of all particles [see Fig. 4(a)]. The maximal energy is close to a_E for both distributions, but for escaping particles it is somewhat lower. The distribution of all particles includes particles moving in the ART regime, which are accelerated by the maximal electric field and gain the largest energy. Particles released from trapping can emit photons near the second and the third electric field nodes, so the maximum and cutoff of their spectrum are shifted to lower energies. At the same time escaping particles do not include particles moving in the NRT regime, therefore, the spectrum of all particles demonstrates more low-energy particles.

The spectrum of escaping particles gives clear evidence of the QED cascade impact. Owing to the cascade a greater portion of particles is accelerated in the region of the strongest electric field. This leads to an increase of the cutoff energy and maximum of the spectrum in comparison with the characteristics obtained without QED cascade. In the last case these characteristics are obtained in frame of Ref. [30], and the location of the maximum is shown by the vertical dashed line in Fig. 4(a).

Photon energy spectra are mainly determined by the particles' energy and the dimensionless quantum parameter χ [38]. When $\chi > 1$, a particle can lose almost all energy in a single act of photon emission. According to Ref. [30] this parameter becomes greater than unity at the power of a few PW. Thus the maximum energy of generated photons is also close to a_E [see Fig. 4(a)]. Also note that the spectrum of escaping photons has a dip in the high-energy range in comparison with the spectrum of all photons in the simulation box [see Fig. 4(a)]. Photons in this energy range are more likely to decay into electron-positron pairs before leaving the focal region. In spite of this dip in spectrum, the QED cascade can lead to a greater number of high-energy photons as a consequence of a greater number of high energy particles in comparison with the case when the QED cascade is switched off (as compared with results in Ref. [30]). A similar effect has been observed in the case of an e-dipole wave at near threshold powers [39].

The QED cascade also qualitatively modifies the angular distribution of particles and photons. Without the cascade particles mainly escape the focal region in the axial direction [30]. Photon decay in the inner region significantly increases the number of particles in the vicinity of the plane $z = 0$. Due to proximity to this plane a major portion of particles do not acquire large axial momentum. Moreover, many of the generated particles become trapped in the ART regime, also leading to transverse escape. As a result, the angular distributions of escaping particles are very narrow with a peak at polar angle $\theta = \pi/2$ and a half of an angular spread of about 1° [see Fig. 4(b)]. Such an angular distribution of particles also makes the photon angular distribution more narrow. At $P = 20$ PW a half of the angular width is around 2° without the cascade [30], and 1° with the cascade [see Fig. 4(b)]. Moreover the cascade makes angular distributions of particles and photons very similar, especially near $\theta \approx \pi/2$. Note that in the case of the e-dipole wave the QED cascade does not change the angular distribution qualitatively at the near threshold power [39,40].

To summarize, in this section we clearly show that since vacuum breakdown strongly affects the pair distribution, the spectra of particles and photons can significantly differ

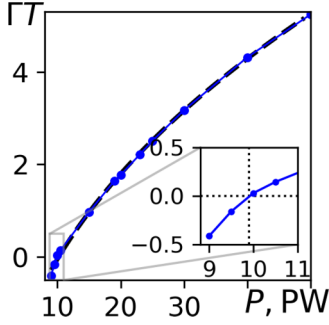


FIG. 5. Dependence of avalanche growth rate in fields of a standing m-dipole wave on wave power. Markers correspond to simulation results. Dashed line shows approximation.

from those obtained at powers when the QED cascade is negligible.

VI. THRESHOLD OF VACUUM BREAKDOWN

In previous sections we considered individual particle motion and the evolution of ensembles of electrons and positrons as a result of the avalanche-like production of pairs in fields of a 10-PW-level m-dipole wave. Based on this knowledge we move on to numerical and analytical estimation of the threshold power of vacuum breakdown, i.e., the amount of total laser power we must deliver to a seed target in order to trigger vacuum breakdown. We refer to this threshold as the minimal total laser power required for a self-sustained QED cascade, i.e., at powers above this value the number of particles grows exponentially in time. Note that in this paper we limit our consideration to the breakdown stage in the conditions when plasma back reaction can be neglected.

A. Numerical results

We performed QED-PIC simulations of interaction of an m-dipole wave with a plasma target for different values of total power. In order to determine the threshold power for vacuum breakdown we calculate the avalanche growth rate $\Gamma = \ln\left(\frac{N_p(t_s + lT)}{N_p(t_s)}\right)/lT$. Here, to reduce statistical error the growth rate is averaged over l laser periods, $N_p(t)$ is the number of electron-positron pairs in the simulation box at the moment of time t , t_s is the moment of time chosen in such a way that the exponential growth of the amount of particles becomes steady. It should be noted that the growth rate Γ is the difference of the production rate of new particles and the rate of particle escape from the focal region. The minimal t_s and l required to achieve reasonable accuracy depend on growth rate and therefore on laser power, but for all our simulations the employed values $t_s = 18T$ and $l = 2$ were sufficient. The growth rate Γ as function of power is depicted in Fig. 5.

First, simulations show that the vacuum breakdown threshold power is $P_{\text{th}} \approx 10$ PW (an inset in Fig. 5). We should also note that although the field structure is different from the e-dipole wave and it seems nonoptimal for triggering of the vacuum breakdown, the threshold powers are comparable: 10 PW in the case of the m-dipole wave versus 7.2 PW in the case of the e-dipole wave [27].

Second, laser fields with an m-dipole structure with power of about 10 PW can produce dense electron-positron plasma on a femtosecond time scale. For example, 2.5 wave periods are required to increase the electron-positron plasma density by two orders of magnitude in fields of a 20 PW m-dipole wave. For $P > 10$ PW a quite accurate approximation of the avalanche growth rate is $\Gamma T = 2.2(P^{0.4} - 2.6)$ (the black dashed line in Fig. 5).

B. Analytical estimate of the threshold

In this paragraph we present simple analytical estimations of the vacuum breakdown threshold. We pay particular attention to cascade development in the inner region and the outer region, as well as consider interdependence of these regions. A comprehensive study based on probability distribution functions for photon emission and decay in highly inhomogeneous fields is practically impossible to perform analytically. Such a study, however, can be performed in frame of QED-PIC simulations, which we also used in order to estimate breakdown threshold powers more accurately. We performed additional numerical simulations with separated regions: the QED cascade was intentionally switched off in the inner or the outer region separated by the imaginary cylindrical surface $\rho = 0.6\lambda$. In the region where the QED cascade was switched off, photon decay was permitted and particles experienced recoil, but the generated pairs and photons were not added to the simulation.

It was shown in the previous paragraph that the vacuum breakdown threshold for an m-dipole wave is approximately 10 PW. One may expect that the most important region for vacuum breakdown is the inner region, where due to the larger electric field particles can gain a larger energy. However, we found that at the same power of 10 PW vacuum breakdown does not occur in any of these regions if inner and outer regions are separated. The absence of vacuum breakdown in the separated regions clearly shows that the inner and outer layers are interconnected and help each other trigger vacuum breakdown.

We start our analysis by recalling the particle quantum parameter $\chi_q \approx \eta \varepsilon_q F_{\perp}$ [38], where the index q defines the type of the particle, namely, p and γ for particle and photon characteristics, respectively, $\eta = \hbar\omega/\varepsilon_0$, \hbar is the Plank constant, ε_q is the particle or photon energy divided by ε_0 , $F_{\perp} = \sqrt{(\mathbf{E} + [\boldsymbol{\beta}_q \times \mathbf{B}])^2 - (\boldsymbol{\beta}_q \cdot \mathbf{E})^2}$ is the effective transverse field, and $\boldsymbol{\beta}_q$ is the particle or photon velocity divided by c , where c is the speed of light.

The particle's parameter χ_p determines which fraction δ of the particle's energy it loses in a single act of photon emission. The average value of this fraction can be expressed as $\bar{\delta} = \int_0^1 \delta \frac{dW_{\gamma}}{d\delta} d\delta / W_{\gamma}$, where W_{γ} is the probability for a particle to emit a photon per unit time, $\frac{dW_{\gamma}}{d\delta}$ is the spectral probability density of photon emission per unit time, and $W_{\gamma} = \int_0^1 \frac{dW_{\gamma}}{d\delta} d\delta$. By analogy with the effective frequency of synchrotron radiation [41] we obtained that in the range $0.17 < \chi_p < 38$ a fairly accurate approximation is $\bar{\delta} = \frac{0.21\chi_p}{2/3 + \chi_p}$ (with better than 10% accuracy).

The photon's parameter χ_{γ} determines how quickly photons can decay. The expression for the probability of photon

decay per unit time is $W_d = \frac{2\alpha}{3^{1.5}\eta\epsilon_\gamma T} \int_0^1 \frac{9-u^2}{1-u^2} K_{2/3}\left(\frac{8/3\chi_\gamma}{1-u^2}\right) du$ [37]. If $\chi_\gamma \ll 1$ then the probability of photon decay per unit time is exponentially small: $W_d = \frac{1.45\alpha}{\eta\epsilon_\gamma T} \chi_\gamma \exp\left(-\frac{8}{3\chi_\gamma}\right)$. This dependence of W_d on χ_γ determines the condition $\chi_\gamma \gtrsim 1$ necessary for vacuum breakdown [10], which is especially relevant in the case of fast particle escape from tightly focused fields. According to our simulations a more accurate condition is $\chi_\gamma > 0.5$. This rough estimate can give a lower bound for the threshold power, but it should be noted that it does not take into account particle and photon escape or particle and photon spectra.

In the inner region close to the electric field antinode the particle Lorentz factor can reach $\gamma_p^{\text{in}} = a_E \approx 510\sqrt{P}$, the quantum parameter can reach $\chi_p^{\text{in}} \approx 0.34a_B\eta\gamma_p^{\text{in}} \approx 0.4P$. Here and below for estimates we consider the magnetic field amplitude as the characteristic transverse field F_\perp , because most of particles and photons mainly propagate close to the $z = 0$ plane [see Figs. 3(a), 3(b), 3(e), and 3(f) and Fig. 4(b)], where the magnetic field is almost transverse to the particle momentum. Moreover, according to trajectory analysis, the magnetic field stimulates photon emission. Since in the considered 10 PW power range $\chi_p^{\text{in}} > 1$, the maximum energy of photons is $\epsilon_\gamma^{\text{in,max}} = \gamma_p^{\text{in}} \approx 510\sqrt{P}$, however, the average photon energy is $\bar{\epsilon}_\gamma^{\text{in}} = \gamma_p^{\text{in}} \bar{\delta}(\chi_p^{\text{in}}) = \frac{125P^{1.5}}{2+1.2P}$, so $\bar{\chi}_\gamma^{\text{in}} = 0.34a_B\eta\bar{\epsilon}_\gamma^{\text{in}} \approx \frac{0.1P^2}{2+1.2P}$. If this region is considered separately, then the necessary condition $\bar{\chi}_\gamma^{\text{in}} > 0.5$ for vacuum breakdown requires $P > 8$ PW.

However, charged particles escape the inner region in $0.5 - 1T$ on average and the characteristic escape time of photons is approximately $l_F/c = 0.4T$ (l_F is the characteristic scale of the field structure). To take into account escape of particles and photons from the focal region we performed a series of numerical simulations with QED cascade switched on only in the inner region. The threshold was determined in a manner similar to the one described in Sec. VI A and amounts to 12.5 PW. It is approximately 1.6 times greater than the threshold power value estimated above because that estimate does not take into account escape of particles and photons.

In the outer region close to the electric field antinode the particle Lorentz factor can reach $\gamma_p^{\text{out}} = 0.4a_E \approx 200\sqrt{P}$, the quantum parameter can reach $\chi_p^{\text{out}} = 0.34a_B\eta\gamma_p^{\text{out}} \approx 0.15P$. Since $\chi_p^{\text{out}} > 1$ at powers of 10-PW-level range, the maximum energy of photons is $\epsilon_\gamma^{\text{out,max}} = \gamma_p^{\text{out}} \approx 200\sqrt{P}$. The average photon energy is $\bar{\epsilon}_\gamma^{\text{out}} = \gamma_p^{\text{out}} \bar{\delta}(\chi_p^{\text{out}}) \approx \frac{18P^{1.5}}{2+0.44P}$, and the average quantum parameter is $\bar{\chi}_\gamma^{\text{out}} = 0.34a_B\eta\bar{\epsilon}_\gamma^{\text{out}} \approx \frac{0.01P^2}{2+0.44P}$. Thus, in the outer region the necessary condition $\bar{\chi}_\gamma^{\text{out}} > 0.5$ dictates that the wave power should be $P > 21$ PW in order to trigger vacuum breakdown. In this region particles require a longer time of several wave periods to leave the trapping region, but photons escape the outer region within $0.25T$. According to the QED-PIC simulations with separated regions, the escape of particles and photons increases the threshold power in the outer region up to 23 PW. The difference between the analytically estimated threshold and the threshold obtained in frame of QED-PIC simulations is smaller in the outer region than in the inner region be-

cause in the former case the particle escape rate is much slower.

The estimates obtained for the outer region and the inner region also allow understanding of the decrease of the vacuum breakdown threshold due to the interplay between these two regions. Particles escape the inner region more quickly on average, so in order to decrease the vacuum breakdown threshold photons from the outer region must decay in the inner region. The energy of these photons is $\bar{\epsilon}_\gamma^{\text{out}}$, and propagating towards the center they can reach the maximum magnetic field a_B where their quantum parameter $\bar{\chi}_{o-i} = a_B\eta\bar{\epsilon}_\gamma^{\text{out}} \approx \frac{0.04P^2}{2+0.44P}$. From the lower estimate $\bar{\chi}_{o-i} > 0.5$ it follows that vacuum breakdown is possible when $P > 8.8$ PW, which is quite close to the vacuum breakdown threshold $P_{\text{th}} \approx 10$ PW given by QED-PIC simulations. Note that photons from the inner region can also decay in the outer region. In this case the photon quantum parameter is $\bar{\chi}_{i-o} = 0.34a_B\eta\bar{\epsilon}_\gamma^{\text{in}} \approx \frac{0.1P^2}{2+1.2P} > 0.5$ when $P > 8$ PW.

To summarize, if the inner region and the outer region are separated, the vacuum breakdown threshold with (with-out) particles escape taken into account can be estimated as 12.5 PW (8 PW) and 23 PW (21 PW) for the inner and the outer region, respectively. This result is in line with our initial guess that the inner region plays a crucial role in vacuum breakdown. However, the interconnection of the outer region and the inner region decreases the threshold power down to 10 PW in simulations with particles escape taken into account. Photons from the outer region can decay in the inner region and compensate fast particle escape. In turn, particles leaving the inner region can be trapped in the outer region. At the same time photons generated in the inner region can decay in the outer region. Thus, during vacuum breakdown pair production occurs in both regions, and at near threshold wave powers the inner and outer layers are equally pronounced.

C. Characteristics of photon production and decay

To illustrate our conclusions with help of numerical simulations, we analyze events of photon emission and photon decay as a function of time, coordinates, energy and the quantum parameter of parent particles or photons. First, we calculate spatiotemporal densities $n_q(\rho, \varphi, z, t)$ of events, where the index q defines the type of event, p and γ for photon decay and photon emission, respectively. Due to axial symmetry we can consider the half-plane $\varphi = 0$ without loss of generality, thus φ can be eliminated from the list of parameters. Based on this event density we calculate the radial distribution $n_q^o(\rho, t) = \int n_q(\rho, z, t) dz$. The obtained quantity reflects the distribution in the central plane, because particle distribution has a small width along the z axis. In order to derive the distribution with respect to another physical quantity A (namely, energy ϵ or quantum parameter χ of the parent particle) we calculate distribution functions $f_q(\rho, z, t, A)$ and introduce event densities $n_q^A(A, t) = \int f_q(\rho, z, t, A) dz d\rho$. Finally, we normalize the obtained distributions to their respective maximum values $\bar{n}_q^v = n_q^v(v, t)/n_q^{v,\text{max}}(v, t)$, where the parameter v defines with respect to which quantity ρ , ϵ , or χ the distribution is ob-

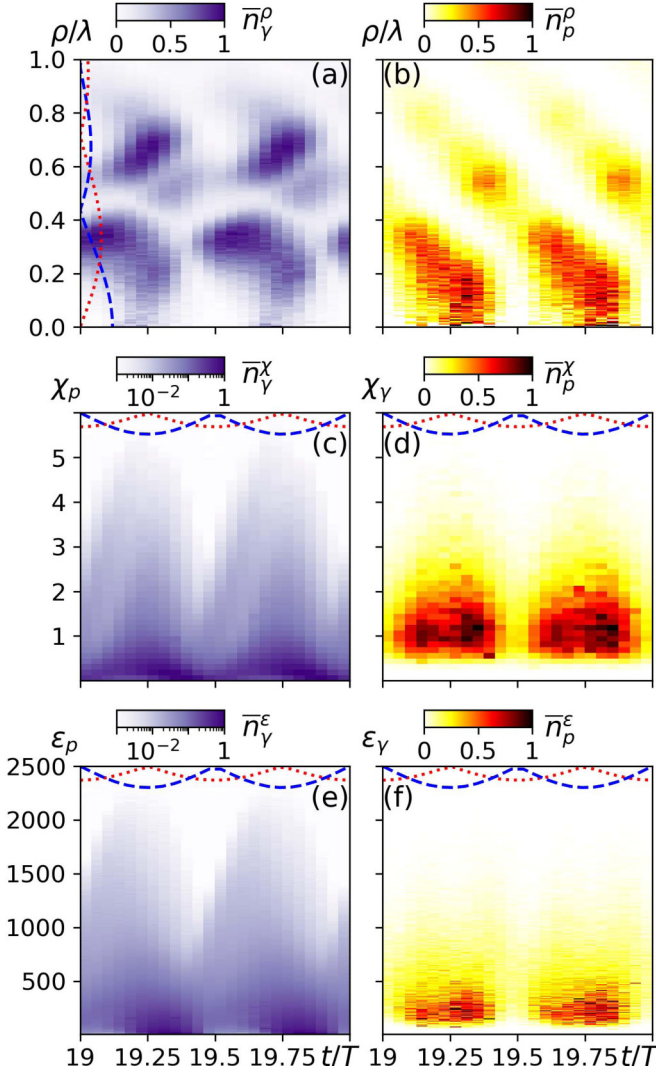


FIG. 6. Normalized distributions of densities of photon \bar{n}_γ and pair \bar{n}_p production as function of time and radial coordinate ρ (a, b); as function of time and parent electron(positron) quantum parameter χ_p (c) or photon quantum parameter χ_γ (d); as function of time and parent electron(positron) energy ϵ_p (e) or photon energy ϵ_γ (f), normalized to the electron rest energy. The dotted red curve and the dashed blue curve correspond in panel (a) to the distribution of electric and magnetic fields along the radial direction in the central plane $z = 0$ and in panels (c–f) to the time evolution of electric and magnetic fields in their first antinodes.

tained. The results of calculations for the near threshold power of 10 PW are shown in Fig. 6.

First of all, radial event distributions in Figs. 6(a) and 6(b) confirm that the surface $\rho = 0.6\lambda$ determined from the particle density distribution can be treated as a boundary between the outer and inner regions. Photon and pair production in both regions is modulated in time, pair and photon production is minimal when the magnetic field is negligible ($t = 0.5kT$, $k \in \mathbb{Z}$), this is also seen from Figs. 6(c)–6(f). Moreover, in the vicinity of the magnetic field node $\rho = 0.44\lambda$ photon production and photon decay are suppressed. These two facts emphasize the role of the magnetic field as the main

component of the effective transverse field F_\perp . Figure 6(b) also helps explain why transverse escape dominates over axial escape during vacuum breakdown. Prominent pair production in the inner region leads to a strong increase of the relative number of particles moving in the ART regime or escaping this region soon after generation. In both cases particles do not gain large axial momentum and escape mainly in the transverse direction.

Analysis of the photon emission distribution with respect to the quantum parameter χ_p in Fig. 6(c) shows that for $P = 10$ PW the maximal quantum parameter of parent particles $\chi_p^{\max} \approx 5$, which is consistent with the maximum value among analytical estimates of χ_p in both regions $\chi_p^{\text{in}} \approx 4$. The photon decay distribution in Fig. 6(d) clearly demonstrates that there are almost no acts of photon decay for $\chi_\gamma^{\min} < 0.5$, so the condition $\chi_\gamma > 0.5$ chosen in Sec. VI B for estimation of the vacuum breakdown threshold is reasonable. The majority of events of photon decay occur with $\chi_\gamma \sim 1$, because for larger χ_γ the number of photons significantly decreases, while for smaller χ_γ the probability of photon decay becomes exponentially small. The maximum photon quantum parameter is approximately the same as for particles and corresponds to photons which take away almost all kinetic energy from particles.

Event distribution with respect to parent particle energy in Fig. 6(e) reveals that the particle energy varies in the range [1; 2300], which is close to the analytical range [1; $\gamma_p^{\text{in}} \approx 1600$] estimated in Sec. VI B. The energy distribution of decayed photons, shown in Fig. 6(f), demonstrates that the majority of photon decay events happen in the range $\epsilon_\gamma \in [150, 650]$, and the maximal photon energy corresponds to the maximal energy of the parent particle. As follows from Sec. VI B, an analytical estimate of the average photon energy in the inner layer $\bar{\epsilon}_\gamma^{\text{in}} \approx 300$ is in the middle of this range. According to Fig. 6(d) photons can decay if $\epsilon_\gamma > 110$. This photon energy corresponds to the minimal quantum parameter ($\chi_\gamma^{\min} = 0.5$) sufficient for photon decay. In the strongest transverse field $F_\perp \approx a_B$ the analytical estimate of the minimal energy from Sec. VI B is $\epsilon_\gamma^{\min} = 0.5/(\eta a_B) \approx 75$, which correlates with the corresponding result of the numerical simulation ($\epsilon_\gamma^{\min} \approx 110$).

To summarize, a qualitative analysis based on analytical estimations and numerical simulations of vacuum breakdown is presented. It explains the interconnection of the inner layer with the outer layer and shows temporal dynamics of photon emission and decay. The derived analytical estimates differ from the values obtained as a result of the numerical simulation by a factor of no larger than 2.

VII. TOWARDS EXPERIMENTAL OBSERVATION OF VACUUM BREAKDOWN

In previous sections we discussed the structure and properties of vacuum breakdown in fields of an m-dipole wave. Given this systematical background, the next important question is: Whether we are able to detect this kind of dynamics in real experimental studies. Here, we would like to highlight important observable properties of vacuum breakdown that

could unequivocally confirm the process of vacuum breakdown under quite reasonable conditions.

It is extremely challenging for experimental detection to resolve the exponential growth of the number of pairs in fields of femtosecond pulses. It is much simpler to register the total number of pairs propagating in a certain direction. However, in general this number of pairs is not a rigorous criterion for detection of vacuum breakdown, because pairs can be generated by seed particles via decay of emitted photons but do not maintain avalanche production due to quick escape from the focal region. For this reason the angular distributions of escaping particles and photons can be the key evidence of vacuum breakdown. Indeed as we showed in Sec. V in the case of a continuous wave, due to the breakdown pairs escape the focal region mainly in directions perpendicular to the axis of field symmetry. At powers below the threshold the main direction of escape is axial. Below we confirm this conclusion in the more realistic case of a pulsed converging dipole wave interacting with a seed target of overcritical density.

The schematic of the proposed experiment setup is the following. A converging m-dipole wave with power between 3 PW and 15 PW and a FWHM pulse duration of 30 fs irradiates a solid density target. This field structure can be realized in an experiment with the help of a number of linearly polarized beams [26,28]. We consider a test hydrogen-like target in the form of a nanowire with a radius of 0.25λ and a density of $10n_c$, where $n_c = m\omega^2/(4\pi e^2) \approx 1.4 \times 10^{21} \text{cm}^{-3}$. Numerical modeling was performed using the QED-PIC code PICADOR [35]. The simulation box has sizes $6\lambda \times 6\lambda \times 6\lambda$ and the number of cells $768 \times 768 \times 768$ along x , y , and z axes, the time step is $T/300$. The target is aligned along the wave symmetry axis (z axis) and the initial number of particles of each type (electrons and ions) is 1.2×10^7 . Radiation losses are modeled as random acts of photon emission with the help of the Adaptive Event Generator [36]. Unlike the previous sections, where the given fields of a standing wave were considered, here the converging dipole wave is generated at the boundary of the simulation box, and the standing structure is formed when this wave reaches the center of simulation region; also, fields produced by particles are taken into account.

The self-consistent dynamics of the interaction of the pulsed m-dipole wave for different powers is demonstrated in Fig. 7. First, particles are pushed to the center by the incoming laser wave; see the left part of the panels in Figs. 7(a), 7(c), and 7(e), where the initial stage of compression is shown. The electron compression stage is similar for all considered pulse powers, and electron density rises up to $700 n_c$. After compression electrons are expelled from the interaction region well before the laser field in the center reaches its maximum value; see Figs. 7(b), 7(d), and 7(f). When the laser field with an established standing wave structure reaches its maximum value at $t \approx 20T$, the electron density already falls down to values comparable to n_c and these remaining particles act as a seed for QED cascade development.

Further dynamics of the electron-positron pair plasma heavily depends on the m-dipole wave power. For a pulse power of 3 PW, which is well below the vacuum breakdown threshold of 10 PW, only a small amount of pairs is produced near the instant of the maximum amplitude and positron density is always lower than electron density. There

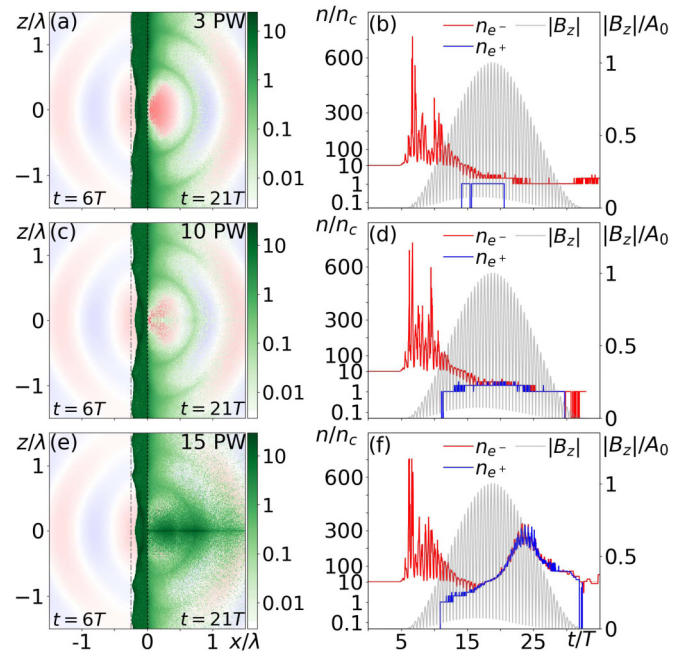


FIG. 7. Irradiation of cylindrical target with radius 0.25λ and density $10n_c$ by m-dipole wave with pulse duration of 30 fs and peak power 3 PW (a, b), 10 PW (c, d), and 15 PW (e, f). (a, c, e) Distributions of electron density n_{e^-} (green) and magnetic field B_z (shaded red-blue) in the plane $y = 0$ for different powers of m-dipole wave. Left part of each panel shows electron density distribution at $t = 6T$ (target compression); right part shows electron density distribution averaged over one laser period at $t = 21T$ (vacuum breakdown for 10 PW and 15 PW). Electron density is normalized to n_c and plotted to a logarithmic scale. Dash-dotted line in left part of each panel depicts initial boundary of target. (b, d, f) Timeline of interaction for different powers of m-dipole wave. Light gray curve depicts absolute value of B_z in the center normalized to maximum amplitude of m-dipole wave A_0 , red and blue curves show maximum electron density n_{e^-} and maximum positron density n_{e^+} in the central plane $z = 0$, respectively. Electron and positron densities are normalized to n_c . Density axis is linear above $10 n_c$ and logarithmic below this value.

is no toroidal structures discussed earlier in case of continuous m-dipole wave [see Fig. 7(a)]. When the wave power is close to the threshold value of 10 PW, pair production starts earlier and electron-positron plasma is created, although its density does not exceed several n_c ; see Fig. 7(d). Note that while the instantaneous power is below the vacuum breakdown threshold of 10 PW, electron-positron pairs can be generated, but they quickly escape the focal region without sustaining the QED cascade. In the spatial distribution only the low density trace of the earlier discussed toroidal structures near the central plane $z = 0$ can be seen in Fig. 7(c). If the laser power exceeds the threshold value, electron-positron pair plasma density grows rapidly and for a 15 PW m-dipole wave reaches the maximum value of $300 n_c$; see Fig. 7(f). This electron-positron pair plasma, depicted in Fig. 7(e), has a toroidal structure in the central plane $z = 0$ close to the one shown in Fig. 3(a). Here we want to stress that although the initial target density is overcritical, it is still well below relativistic critical density γn_c (for a 15 PW m-dipole wave the maximum

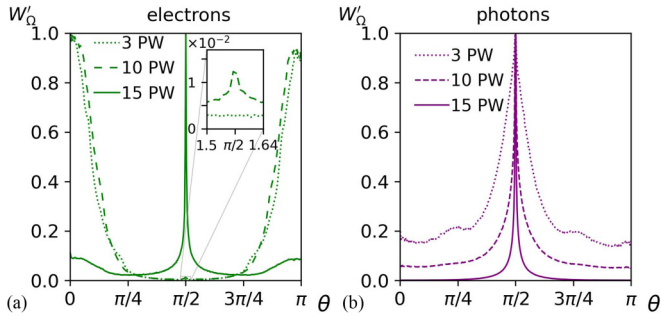


FIG. 8. Signatures of vacuum breakdown in fields of an m-dipole wave. Angular distributions of escaping (a) electrons and (b) gamma photons as a result of irradiation of cylindrical target with radius 0.25λ and density $10n_c$ by the pulsed m-dipole wave with peak power 3 PW, 10 PW, 15 PW and FWHM pulse duration of 30 fs.

γ is approximately 2000). For the considered laser pulses with a realistic pulse duration of 30 fs pair density during interaction is also below the relativistic critical density value throughout the whole simulation, which is confirmed by the unchanged field profile in Figs. 7(b), 7(d), and 7(f). Thus, the further discussed behavior of the angular distribution characterizes the spatial redistribution of particles during the vacuum breakdown process and does not originate from self-consistent interaction of laser radiation with dense plasma.

In order to reveal vacuum breakdown signatures in the case of a pulsed wave we propose to employ angular characteristics of emitted photons and charged particles. We track escaping charged particles and gamma photons crossing the observation sphere with a radius of 3λ during the whole simulation time. The angular distribution W'_Ω denotes the total energy of particles or photons, which crossed the observation sphere with momentum directed into an element of solid angle. In Fig. 8 the distributions normalized to their maxima $\overline{W'_\Omega} = W'_\Omega/W'_\Omega^{\max}$ are presented. As can be seen from the figure, there are two main effects that can be observed. The first one is that the angular distribution of electrons is completely different for 3 PW and 15 PW, as shown in Fig. 8(a). The second effect is that the angular distribution of photons becomes much narrower with increase of wave power; see Fig. 8(b).

These effects can be qualitatively explained based on particle trajectory analysis [30]. At lower power $P < 10$ PW, when there is no vacuum breakdown, particles escape mainly along the z axis, photons escape in the transverse direction and radiation losses lead to approximately twice the angular spread for particles and half the angular spread for photons. It was shown in previous sections that at powers exceeding the threshold of vacuum breakdown (~ 10 PW) particles become distributed closer to the plane $z = 0$ and many of the generated pairs are trapped in the ART regime leading to the domination of radial escape, so charged particles leave the interaction region mainly in the transverse direction. It can be seen in Fig. 7(c) that for the 10 PW pulsed m-dipole wave there are few particles in the central plane $z = 0$, so the angular

distribution remains nearly unchanged in comparison with the 3 PW wave except for the small peak near $\pi/2$ shown in the inset in Fig. 8(a). For higher powers, e.g., a 15 PW wave, this type of trajectories in the central plane $z = 0$ becomes dominant as shown in Fig. 7(e). Thus, the angular distribution of charged particles drastically changes, while the photons' angular distribution becomes much narrower when wave power exceeds the breakdown threshold. These two observations, if detected, can be treated as experimental evidence of vacuum breakdown in a pulsed converging m-dipole wave.

VIII. CONCLUSIONS

In this paper we have studied vacuum breakdown in laser fields in the form of a converging m-dipole wave, which maximizes the magnetic field, in the 10 PW power range with the help of QED-PIC simulations. The main attention has been paid to the avalanche stage of QED cascade development when the generated electron-positron plasma has a low density insufficient to influence back on the driving laser wave. Based on trajectory analysis we demonstrate how this process originates as a balance of two competing processes: particle production due to QED cascade and particle escape from a highly nonuniform field. The space-time distribution of plasma has the form of concentric oscillating toroidal layers and is determined not only by the space-time structure of pair production but also by particle motion. In this power range newly born particles can quickly escape the focal region or be trapped in the electric field node (outer) region. Trapped particles abundantly emit photons in the direction towards the focus and due to photon decay the region around the first electric field antinode (inner region) is also populated by electrons and positrons. The nonlocality of the QED cascade is of great importance and the coupling of these two regions determines the threshold power of vacuum breakdown which is approximately 10 PW. Angular and spectral properties of charged particles and gamma photons are discussed. In particular, it is shown that since the QED cascade develops mainly in the central plane, the angular distribution has a distinct peak in the transverse direction for both photons and charged particles. Based on the analysis of particle motion and the corresponding angular distributions we propose a way to experimentally observe unambiguous evidence of vacuum breakdown in the case of a pulsed m-dipole wave modeled by several laser beams.

ACKNOWLEDGMENTS

The authors would like to acknowledge the support by the Ministry of Science and Higher Education of the Russian Federation, Agreement No. 075-15-2021-633 (analysis of particle trajectories) and by the RFBR and ROSATOM according to the research Project No. 20-21-00095 (space-time structure and threshold of vacuum breakdown, experimental evidence of vacuum breakdown). The authors acknowledge the use of computational resources provided by the Joint Supercomputer Center of the Russian Academy of Sciences.

- [1] Y. Raizer, *Laser-Induced Discharge Phenomena* (Consultants Bureau, New York, 1977).
- [2] C. N. Danson, C. Haefner, J. Bromage, T. Butcher, J.-C. F. Chanteloup, E. A. Chowdhury, A. Galvanauskas, L. A. Gizzi, J. Hein, D. I. Hillier *et al.*, *High Power Laser Sci. Eng.* **7**, e54 (2019).
- [3] M. Marklund and P. K. Shukla, *Rev. Mod. Phys.* **78**, 591 (2006).
- [4] A. Di Piazza, C. Müller, K. Z. Hatsagortsyan, and C. H. Keitel, *Rev. Mod. Phys.* **84**, 1177 (2012).
- [5] J. Schwinger, *Phys. Rev.* **82**, 664 (1951).
- [6] A. M. Fedotov, *Laser Phys.* **19**, 214 (2009).
- [7] S. S. Bulanov, V. D. Mur, N. B. Narozhny, J. Nees, and V. S. Popov, *Phys. Rev. Lett.* **104**, 220404 (2010).
- [8] A. Gonoskov, I. Gonoskov, C. Harvey, A. Ilderton, A. Kim, M. Marklund, G. Mourou, and A. Sergeev, *Phys. Rev. Lett.* **111**, 060404 (2013).
- [9] A. R. Bell and J. G. Kirk, *Phys. Rev. Lett.* **101**, 200403 (2008).
- [10] A. M. Fedotov, N. B. Narozhny, G. Mourou, and G. Korn, *Phys. Rev. Lett.* **105**, 080402 (2010).
- [11] S. S. Bulanov, T. Z. Esirkepov, A. G. R. Thomas, J. K. Koga, and S. V. Bulanov, *Phys. Rev. Lett.* **105**, 220407 (2010).
- [12] E. N. Nerush, I. Y. Kostyukov, A. M. Fedotov, N. B. Narozhny, N. V. Elkina, and H. Ruhl, *Phys. Rev. Lett.* **106**, 035001 (2011).
- [13] A. A. Mironov, N. B. Narozhny, and A. M. Fedotov, *Phys. Lett. A* **378**, 3254 (2014).
- [14] V. F. Bashmakov, E. N. Nerush, I. Y. Kostyukov, A. M. Fedotov, and N. B. Narozhny, *Phys. Plasmas* **21**, 013105 (2014).
- [15] W. Luo, Y.-B. Zhu, H.-B. Zhuo, Y.-Y. Ma, Y.-M. Song, Z.-C. Zhu, X.-D. Wang, X.-H. Li, I. C. E. Turcu, and M. Chen, *Phys. Plasmas* **22**, 063112 (2015).
- [16] H. X. Chang, B. Qiao, Z. Xu, X. R. Xu, C. T. Zhou, X. Q. Yan, S. Z. Wu, M. Borghesi, M. Zepf, and X. T. He, *Phys. Rev. E* **92**, 053107 (2015).
- [17] M. Vranic, T. Grismayer, R. A. Fonseca, and L. O. Silva, *Plasma Phys. Control. Fusion* **59**, 014040 (2017).
- [18] T. Grismayer, M. Vranic, J. L. Martins, R. A. Fonseca, and L. O. Silva, *Phys. Rev. E* **95**, 023210 (2017).
- [19] A. V. Bashinov, P. Kumar, and A. V. Kim, *Quantum Electron.* **48**, 833 (2018).
- [20] A. Sampath and M. Tamburini, *Phys. Plasmas* **25**, 083104 (2018).
- [21] D. D. Sorbo, D. R. Blackman, R. Capdessus, K. Small, C. Slade-Lowther, W. Luo, M. J. Duff, A. P. L. Robinson, P. McKenna, Z.-M. Sheng *et al.*, *New J. Phys.* **20**, 033014 (2018).
- [22] Z. Léczy and A. Andreev, *Plasma Phys. Control. Fusion* **61**, 045005 (2019).
- [23] A. S. Samsonov, E. N. Nerush, and I. Y. Kostyukov, *Sci. Rep.* **9**, 11133 (2019).
- [24] M. Jirka, O. Klimo, M. Vranic, S. Weber, and G. Korn, *Sci. Rep.* **7**, 15302 (2017).
- [25] I. Gonoskov, A. Aiello, S. Heugel, and G. Leuchs, *Phys. Rev. A* **86**, 053836 (2012).
- [26] A. Gonoskov, A. Bashinov, I. Gonoskov, C. Harvey, A. Ilderton, A. Kim, M. Marklund, G. Mourou, and A. Sergeev, *Phys. Rev. Lett.* **113**, 014801 (2014).
- [27] A. Gonoskov, A. Bashinov, S. Bastrakov, E. Efimenko, A. Ilderton, A. Kim, M. Marklund, I. Meyerov, A. Muraviev, and A. Sergeev, *Phys. Rev. X* **7**, 041003 (2017).
- [28] E. S. Efimenko, A. V. Bashinov, S. I. Bastrakov, A. A. Gonoskov, A. A. Muraviev, I. B. Meyerov, A. V. Kim, and A. M. Sergeev, *Sci. Rep.* **8**, 2329 (2018).
- [29] E. S. Efimenko, A. V. Bashinov, A. A. Gonoskov, S. I. Bastrakov, A. A. Muraviev, I. B. Meyerov, A. V. Kim, and A. M. Sergeev, *Phys. Rev. E* **99**, 031201(R) (2019).
- [30] A. V. Bashinov, E. S. Efimenko, A. A. Muraviev, V. D. Volokitin, I. B. Meyerov, G. Leuchs, A. M. Sergeev, and A. V. Kim, *Phys. Rev. E* **105**, 065202 (2022).
- [31] A. Hewish, *Rev. Mod. Phys.* **47**, 567 (1975).
- [32] F. C. Michel, *Rev. Mod. Phys.* **54**, 1 (1982).
- [33] V. S. Beskin, *Phys. Usp.* **61**, 353 (2018).
- [34] E. G. Gelfer, *Quantum Electron.* **46**, 310 (2016).
- [35] I. A. Surmin, S. I. Bastrakov, E. S. Efimenko, A. A. Gonoskov, A. V. Korzhimanov, and I. B. Meyerov, *Comput. Phys. Commun.* **202**, 204 (2016).
- [36] A. Gonoskov, S. Bastrakov, E. Efimenko, A. Ilderton, M. Marklund, I. Meyerov, A. Muraviev, A. Sergeev, I. Surmin, and E. Wallin, *Phys. Rev. E* **92**, 023305 (2015).
- [37] V. N. Bayer, V. M. Katkov, and V. S. Fadin, *Radiation of the Relativistic Electrons* (Atomizdat, Moscow, 1973).
- [38] A. I. Nikishov and V. I. Ritus, *Zh. Eksp. Teor. Fiz.* **46**, 776 (1964) [*Sov. Phys. JETP* **19**, 529 (1964)].
- [39] A. V. Bashinov, E. S. Efimenko, A. A. Gonoskov, A. V. Korzhimanov, A. A. Muraviev, A. V. Kim, and A. M. Sergeev, *J. Opt.* **19**, 114012 (2017).
- [40] A. V. Bashinov, P. Kumar, and E. S. Efimenko, *Quantum Electron.* **49**, 314 (2019).
- [41] V. B. Berestetskii, E. M. Lifshits, and L. P. Pitaevskii, *Quantum Electrodynamics* (Pergamon Press, New York, 1982).